Magnetic-order-mediated carrier and phonon dynamics in $MnBi_2Te_4$

L. Cheng [1,2,*] T. Xiang,[1,*] and J. Qi [1,†]

[1]*State Key Laboratory of Electronic Thin Films and Integrated Devices, University of Electronic Science and Technology of China, Chengdu 610054, China*

[2]*Institute of Electronic and Information Engineering of UESTC in Guangdong, Dongguan 523808, China*

(Received 13 July 2023; accepted 19 March 2024; published 22 April 2024)

We investigate the quasiparticle dynamics in $MnBi_2Te_4$ single crystals using ultrafast optical spectroscopy. Our results show that there exist anomalous dynamical optical responses below the antiferromagnetic (AFM) ordering temperature T_N. In specific, we reveal that both the initial carrier decay and recombination processes can be modulated via introducing the AFM order in subpicosecond and picosecond timescales, respectively. We also discover a long relaxation process emerging below T_N with a timescale approaching the nanosecond regime, and can be attributed to the T-dependent spin-lattice interaction. There also emerges an unusual phonon energy renormalization below T_N, which is found to arise from its coupling to the spin degree via the exchange interaction and magnetic anisotropy. Our findings provide key information for understanding the dynamical properties of nonequilibrium carrier, spin, and lattice in $MnBi_2Te_4$.

DOI: 10.1103/PhysRevResearch.6.023073

I. INTRODUCTION

Magnetic order is one of the essential elements for manipulating quantum materials due to its capability of mediating the abundant spin-related phenomena [1–3], as exemplified in strong correlated systems, magnetic two-dimensional materials, as well as the highly focused magnetic topological materials. Their promising applications, e.g., spintronic devices, photonics, and quantum information, are based on the research of interactions between magnetism and related degrees of freedom [3,4]. $MnBi_2Te_4$, a three-dimensional (3D) antiferromagnetic (AFM) topological insulator (TI), is very suitable for studying the interaction between the magnetic order and fermionic carriers in the topological nontrivial band. It has a van der Waals–type layered structure with the space group $R\bar{3}m$ [5,6]. Previous theoretical calculation and experiments show that its Néel temperature (T_N) is around 24 K, below which the AFM order along crystallographic c axis occurs [5,7–9]. Compared to conventional nonmagnetic TIs, the $MnBi_2Te_4$ is also expected to be ideal for exploring exotic topological quantum phenomena such as quantum anomalous Hall effect, axion insulator states, etc. [5,7–15], where it is critical to understand how the charge and lattice degrees of freedom interact with the magnetic order below the transition temperature in this system. The spin-lattice interaction below T_N is found to play the key role for the A_{1g}^1 phonon mode with terahertz frequency, deviating from the anharmonic model in both the bulk $MnBi_2Te_4$ [16] and few-layer $MnBi_2Te_4$ flakes [17], where, however, there exists discrepancy of the reported T-dependent behaviors. Besides, it is still unclear whether the low-energy phonons with gigahertz frequency can be coupled to the spin system [18]. Consequently, several issues remain to be elucidated in this material system, e.g., (1) interaction between the nonequilibrium carriers and the magnetic order, and (2) the spin-lattice coupling in various timescales or energy scales.

Ultrafast optical pump-probe spectroscopy (UOPP) has been proved to be a very effective technique in studying the coupling between different degrees of freedom in the ultrafast timescale, including the charge, phonon, as well as spin or magnon. In this work, we perform temperature-dependent UOPP measurements in $MnBi_2Te_4$ single crystals to study the carrier and lattice dynamics, which are discovered to be strongly coupled with the AFM order below T_N. We discuss quantitatively the relevant interactions contributing to the observed dynamics.

II. EXPERIMENT

Figure 1(a) shows the schematic of our experimental setup, which is commonly used for UOPP measurements. The time-resolved transient reflectivity change $\Delta R/R$ was measured based on a pump-probe scheme using a Ti:sapphire laser oscillator that produces 35-fs pulses with a repetition rate of 80 MHz at a center wavelength of 800 nm ($\sim$1.55 eV). The pump beam, with a typical fluence of $\sim$0.3 $\mu J/cm^2$, directs along the normal incidence and is kept p-polarized. Meanwhile, the probe beam, with a typical fluence of $\sim$0.03 $\mu J/cm^2$, is incident at a $\sim 10^\circ$ angle to the sample normal and is kept s-polarized. In our measurements, the sample temperature can be tuned between 5 K and 300 K

*These authors contributed equally to this work.
†jbqi@uestc.edu.cn

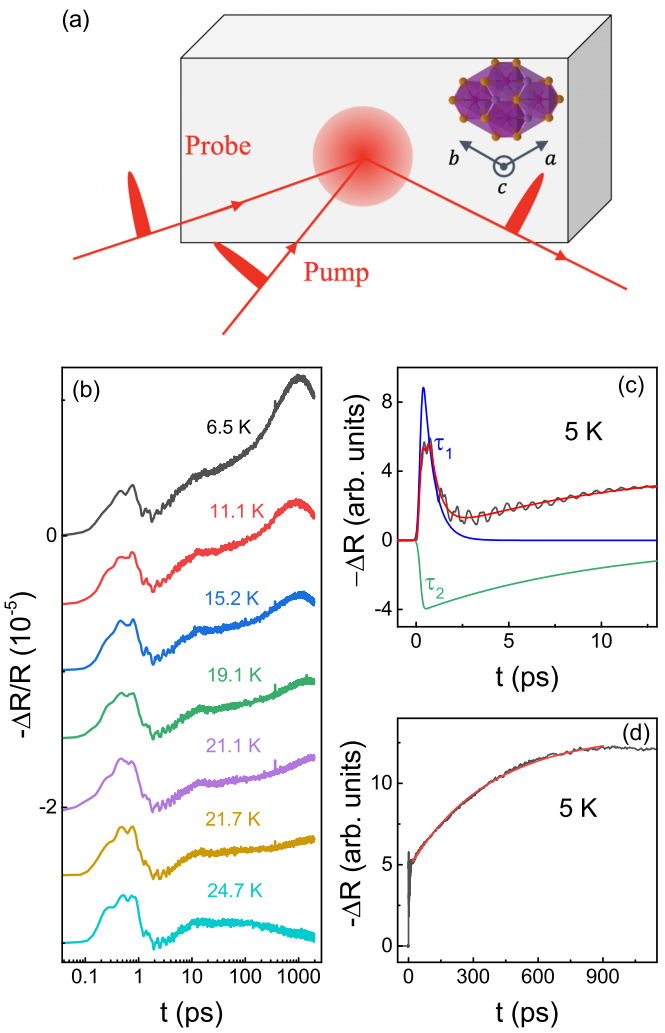

FIG. 1. (a) Schematic picture of the ultrafast optical pump-probe spectroscopy setup. (b) Transient reflectivity $\Delta R(t)/R$ as a function of temperature for bulk $MnBi_2Te_4$ single crystal. (c) Fitting of the nonoscillatory signal at 5 K in short timescale. (d) Fitting of the long-rising component at 5 K in long timescale.

in vacuum. The single-crystal $MnBi_2Te_4$ sample was synthesized by flux method, and characterized by x-ray diffraction (XRD) and Raman spectroscopy measurements. Details about the sample preparation and its characterization are given in Appendix A.

III. RESULTS AND DISCUSSION

Figure 1(b) shows the measured signal $\Delta R/R$ as a function of temperature. Upon photoexcitation, we observe an instantaneous rise followed by a nonoscillatory relaxation superimposed with oscillatory signals. The relaxation components exhibit several decays with different lifetimes, indicating multiple relaxation channels for the photoexcited carriers. Surprisingly, after ∼10 ps below the Néel temperature, there emerges a very slow rising process extending into the nanosecond regime, characterized by τ_{long}.

In fact, the signals $\Delta R/R$ within the initial ∼10 ps are quite similar to those measured in other topological insulators, e.g., Bi_2Se_3 [19–21], where the oscillatory and exponential decay processes could also be found. This is understandable considering that the $MnBi_2Te_4$ belongs to the 3D topological insulator Bi_2Se_3 family with layered structure. In these materials, the short-lifetime decay process is usually related to carrier relaxations, such as carrier cooling or recombination, while the oscillatory components represent the coherent phonon or other collective excitation. They will be discussed in detail below.

First, we focus on the relaxation processes within the initial ∼10 ps. To quantify these decays, we fit the signals with following formula [22,23]:

$$\frac{\Delta R(t)}{R} = \left(\sum_{i=1,2} A_i e^{-\frac{t}{\tau_i}} + C\right) \otimes G(t), \tag{1}$$

where A_j and τ_j $(j = 1, 2)$ are the amplitudes and relaxation times, respectively. C is a constant representing long-lifetime processes, and $G(t)$ is a Gaussian function standing for the pump-probe cross correlation. The fitting quality is very good, as manifested by Fig. 1(c), where we can see that $A_1 < 0$ with τ_1 having a subpicosecond timescale (blue curve), and $A_2 > 0$ with τ_2 having a timescale of few picoseconds (green curve).

The decay time τ_1 as a function of temperature is shown in Fig. 2(a). τ_1 above T_N with a subpicosecond timescale is usually attributed to electron-phonon scattering [21,24,25]. Quantitatively, it could be described by the two-temperature model (TTM) [21,24,25] (see Appendix B), which was previously used to study the relaxation dynamics of photoexcited carriers in metals or semimetals.

As seen in Fig. 2(a), the fitting quality via the TTM is excellent and proves its validity to describe the fast relaxation process characterized by τ_1 at $T > T_N$. We can obtain the electronic specific heat coefficient $\gamma = 4.5$ $\text{Jm}^{-3}\text{K}^{-2}$ and the electron-phonon (e-ph) coupling constant $g_\infty = 8.9 \times 10^{15}$ $\text{Wm}^{-3}\text{K}^{-1}$. These fitted parameters are close to those of the 3D topological insulators in the Bi_2Se_3 family [21], indicating their similar electron-phonon interaction.

Particularly, we notice that τ_1 decreases rapidly below the Néel temperature. The sudden change of τ_1 near T_N clearly cannot be explained by the conventional TTM. Due to the AFM phase transition appearing below T_N, the magnetic order should strongly affect the carrier relaxation [26,27]. Specifically, at $T < T_N$, values of τ_1 are clearly smaller than those expected by the conventional TTM, suggesting that formation of the AFM order opens a new relaxation channel for the hot electrons, which might arise from the electron-magnon interaction [28]. This type of relaxation could be estimated by simply considering the heat exchange between electron and spin subsystems. The associated decay time τ_{em} can be estimated by [29]

$$\tau_{em}^{-1} \propto g_{\text{E-S}}\left[\frac{1}{C^{\text{E}}(T)} + \frac{1}{C^{\text{S}}(T)}\right], \tag{2}$$

where $g_{\text{E-S}}$, $C^{\text{E}}(T)$, and $C^{\text{S}}(T)$ are the electron-magnon coupling constant and specific heat of electron and spin reservoirs, respectively. Here, $C^{\text{E}}(T) = \gamma T_e$, which is obtained from TTM fitting, the temperature T is the ambient temperature, and T_e is the electron temperature (see Appendix B).

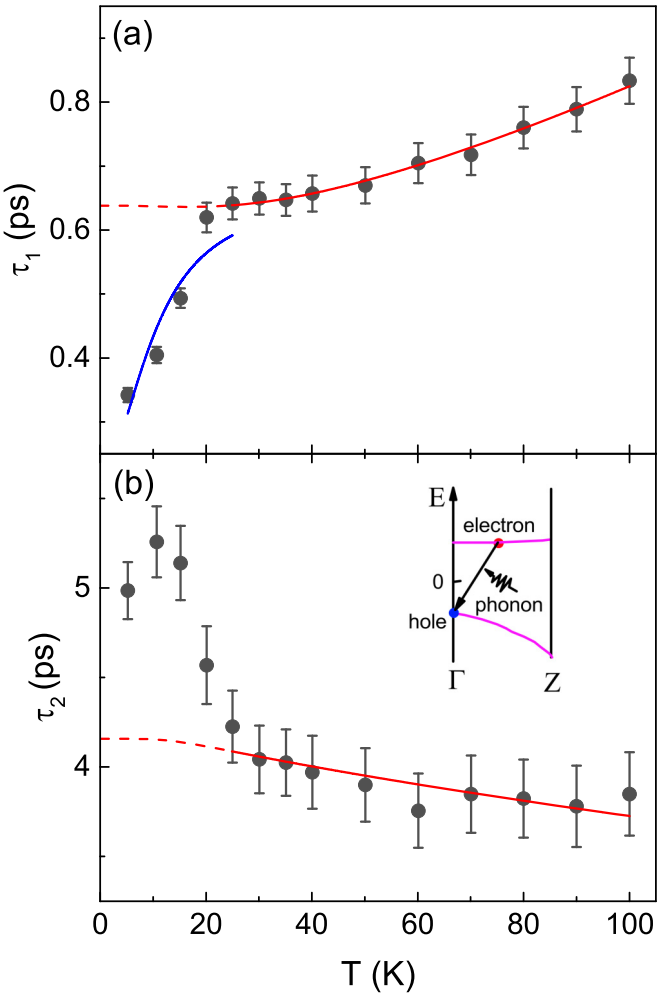

FIG. 2. The decay times τ_1 (a) and τ_2 (b) as a function of temperature. The red solid curve in (a) is the TTM fitting at $T > T_N$ and the dashed curve is the extension to below T_N. The blue solid curve is the fitting via electron-magnon interaction for $T < T_N$. In (b), the red curve is the fitting based on the phonon-assisted e-h recombination process, which is schematically shown by the inset.

Values of $C^{\mathrm{S}}(T)$ are from previous heat capacity measurements [8,30]. In fact, due to $C^{\mathrm{E}}(T) \gg C^{\mathrm{S}}(T)$, we can ignore the term $1/C^{\mathrm{E}}(T)$ in Eq. (2). Therefore, we can fit the values of τ_1 below T_N using the formula $\tau^{-1} = \tau_{em}^{-1} + \tau_c^{-1}$, where τ_c^{-1} represents the contribution from the temperature-insensitive relaxation channel, which is often attributed to e-ph coupling at low temperatures [21,31]. As shown in Fig. 2(a), the fitted results agree well with the experimental data. It is worth mentioning that we treat the value of $g_{\mathrm{E-S}}$ as a constant during the fitting. However, deviation of the fitting curve from the experimental data as T approaches T_N might indicate the temperature-dependent property of $g_{\mathrm{E-S}}$, e.g., gradual vanishing of $g_{\mathrm{E-S}}$ caused by the diminishing of long-range magnetic order. Moreover, considering the analogy between electrons and phonons, we can further estimate the product of dimensionless electron-magnon coupling constant and the square of magnon cut-off frequency $(\lambda_m \omega_m^2)$ to be 42.1 THz^2, according to $\tau_{em} = 5\pi k_B T_e / 3\hbar\lambda_m \omega_m^2$ [28]. Although there is no known parameter value(s) for

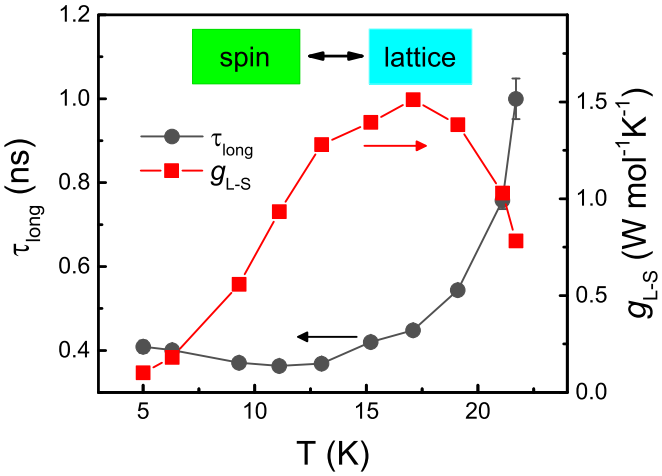

FIG. 3. τ_{long} and g_{L-S} as functions of temperature.

comparison due to the lack of related work from other research groups, such value should be useful for future related research.

τ_2 as a function of temperature, characterizing the decay process with a timescale of several picoseconds, is shown in Fig. 2(b). As is known, after e-ph thermalization, the nonequilibrium electrons (holes) can cool down and accumulate at the minimum (maximum) of the conduction (valence) band. The subsequent relaxation involves the recombination processes. Since direct recombination normally takes a long time with a nanosecond timescale [32], it cannot account for the T-dependent τ_2. However, the phonon-assisted electron-hole (e-h) recombination [24,25,33], where the electron and hole recombine with the assistance of e-ph scattering between the electron and hole pockets, has exactly the same timescale as that of τ_2. Actually, in the electronic structure of single-crystal $MnBi_2Te_4$, the conduction band can be very flat along some specific momentum direction within the Brillouin zone, i.e., bands along $\Gamma - Z$ in the inset of Fig. 2(b) [34], which is in favor of such indirect recombination. Therefore, we can use the phonon-assisted e-ph recombination model to describe the decay time τ_2 as

$$\frac{1}{\tau_2} = A\frac{x}{\sinh^2 x} + \frac{1}{\tau_0}, \tag{3}$$

where $x = \hbar\omega_r / 2k_B T$, and ω_r corresponds to the average frequency of phonons involved in the e-h recombination. τ_0 represents a temperature-independent recombination time which relies on the impurities or defects of the sample. A is a parameter related to the density of states in the electronic energy bands and the matrix elements for interband e-h scattering. It can be seen from Fig. 2(b) that the fitted results agree quite well with the experimental τ_2 above the Néel temperature. We further obtain that $\omega/2\pi = 1.38$ THz and $\tau_0 = 4.16$ ps. Here, ω is quite close to frequency of the dominant oscillation observed [as shown in Figs. 4(a)–4(c)], i.e., A_{1g}^1 mode.

Similar to the temperature-dependent τ_1, the values of τ_2 at $T < T_N$ deviate from the trend predicted by the indirect recombination scenario. Due to the existence of the long-range AFM order in this temperature regime, two possible

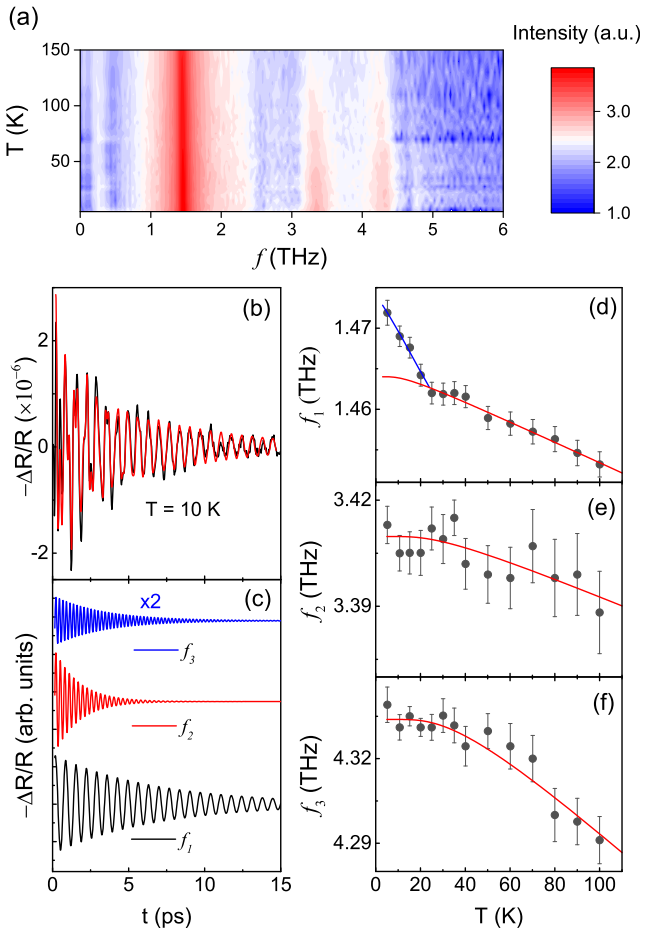

FIG. 4. (a) Fourier transform spectra of the extracted oscillations as a function of temperature (map color rescaled via $\log_2$). (b) Extracted oscillation at 10 K (black) and the fitted curve (red) using damped harmonic oscillators. (c) The three oscillation components with different frequencies derived from the fitting. [(d)–(f)] The frequencies of three phonon modes obtained via fitting as a function of temperature. The red lines are fitted curves using Eq. (5). The blue line in (d) is the fit via Eq. (9).

mechanisms might contribute to such temperature dependence. First, we can consider the interaction between phonons and magnons [16], which can renormalize the phonon frequency and change its population, and hence is able to affect the phonon-assisted recombination. Second, the magnon-assisted recombination can also contribute to the carrier relaxation, where the magnon plays a similar role to the phonon, i.e., compensates the conservation of energy and momentum in the recombination process. However, in the second case magnon should open a new relaxation channel that will accelerate the recombination process. This is clearly not consistent with our observation. Therefore, we believe that the phonon-magnon interaction, rather than the magnon-assisted recombination, dominates the relaxation characterized by τ_2 at $T < T_N$. Renormalization of the phonon energy is indeed observed in our experiment, as discussed in detail below.

As mentioned earlier, after ∼10 ps there emerges a long-rising process below Néel temperature characterized by τ_{long}, which should originate from the AFM order [29,35–37]. Its T-dependent timescale spans from hundreds of picoseconds to a nanosecond, and is consistent with previous observation associated with the spin-lattice interaction in several other magnetic materials [29,35]. This type of interaction could be phenomenologically described by the energy exchange between spin and lattice subsystems [29]. Their coupling can be effectively described by a parameter $g_{\text{L-S}}$, which indicates the coupling strength or energy transfer rate. Then, the relaxation time of nonequilibrium coupled spin-lattice system can be characterized by a decay time [29]:

$$\tau_{\text{long}}^{-1} \propto g_{\text{L-S}}(T)\left[\frac{1}{C^{\text{L}}(T)} + \frac{1}{C^{\text{S}}(T)}\right]. \tag{4}$$

Here, the $C^{\text{L,S}}$ are the phonon and spin heat capacity of the two reservoirs, and their values are from previous heat capacity measurements [8,30]. Values of τ_{long} can be obtained via the single exponential fit to the experimental data with long timescale, as shown in Fig. 3, where a divergence-like behavior near T_N can be seen. Since C^S peaks around T_N, such a phenomenon can be understood via Eq. (4). It is worth noting that in the long lifetime process, the electronic coupling can usually be omitted due to the very small electronic specific heat at low temperatures, and also explains why it is typically addressed in short lifetime processes in prior researches [28,38].

According to the τ_{long}, we can further obtain the coupling coefficient $g_{\text{L-S}}$ as a function of temperature for $MnBi_2Te_4$ below T_N, using the specific heat C^{L} and C^{S} extracted from previous heat capacity measurements [8,30]. Surprisingly, $g_{\text{L-S}}$ does not show a monotonic behavior as a function of temperature below T_N, and it maximizes around a critical temperature $T^* \sim 17$ K. Phenomenologically, below T^* its increasing with T could be attributed to the increment of phonon population, while above T^* its reduction with increasing T should arise from the magnetization $M(T)$ vanishing gradually when approaching T_N. Moreover, due to the long lifetime of this spin-lattice interaction process, the involved collective excitation in the scatterings should have low-energy scales, e.g., acoustic phonon and sub-meV magnon. Since the AFM order is along the out-of-plane direction, its associated magnetic excitation should have the strongest coupling with modes vibrating along the c axis.

Fourier transform spectra of the oscillations extracted from the nonoscillatory $\Delta R/R$ components are shown in Fig. 4(a). Three coherent optical phonon modes in $MnBi_2Te_4$ can be clearly seen, and manifested by a pronounced peak, $f_1 \sim 1.5$ THz, and two smaller peaks, $f_2 \sim 3.4$ THz and $f_3 \sim 4.3$ THz, respectively. These modes are consistent with the previous Raman spectroscopy studies [16,17,39], and can be assigned as A_{1g}^1 (f_1), A_{1g}^2 (f_2), and A_{1g}^3 (f_3) modes, respectively.

The data could be fitted well by three damped harmonic oscillators [40]. A typical example is demonstrated in Figs. 4(b) and 4(c). The obtained temperature-dependent frequencies $f_j(T)$ ($j = 1, 2, 3$) are illustrated in Figs. 4(d)–4(f), which show clear softening with increasing temperature and usually can be explained by the anharmonic phonon model [40–42], where the T-dependent phonon frequency $\omega_A(= 2\pi f_A)$ is

given by

$$\omega_A(T) = \omega_0 + a\left[1 + 2n_B\left(\frac{\omega_0}{2}, T\right)\right], \tag{5}$$

where ω_0 is the intrinsic frequency, and a is the fitting parameter. $n_B(\omega, T) = [e^{\hbar\omega/k_BT} - 1]^{-1}$ is the Bose-Einstein distribution function. We can see that the T-dependent phonon frequencies follow this model in general. However, as shown in Fig. 4(d), it can only describe the T-dependent f_1 for temperatures larger than $\sim T_N$, while it fails to predict the behavior of $f_1(T)$ at lower temperatures. Such a result agrees with the measurements via Raman spectroscopy [16,17]. Since the A_{1g}^1 mode represents the interlayer atomic vibrations along the crystallographic c axis, modulation of the interlayer exchange interaction and anisotropy constant becomes easily achievable. This leads to the spin-lattice coupling effect, which will renormalize the energy of related phonons or magnons.

We can understand such phonon renormalization by incorporating the linear-chain model in $MnBi_2Te_4$ [43], i.e., the Hamiltonian with a phonon can be written as

$$H = \frac{1}{2}\omega_0^2 u^2 + J\sum_{i=1}^{N-1}\vec{M}_i \cdot \vec{M}_{i+1} - \frac{1}{2}K\sum_{i=1}^{N}(\vec{M}_i \cdot \hat{z})^2, \tag{6}$$

where u is the normal coordinate. J is the exchange interaction. $\vec{M}_i$ is the magnetization in the ith layer. $K\,(>0)$ is easy-axis anisotropy energy along the z direction (or c axis). N is the number of septuple layers. We then can solve the phonon frequency for f_1 mode via $\omega_1^2 = d^2H/du^2$:

$$\omega_1^2(T) = \omega_0^2 + \frac{d^2J}{du^2}\sum_{i=1}^{N-1}\vec{M}_i \cdot \vec{M}_{i+1} - \frac{1}{2}\frac{d^2K}{du^2}\sum_{i=1}^{N}(\vec{M}_i \cdot \hat{z})^2. \tag{7}$$

Under the approximation of small displacement, J and K can be written as $J(u) = J_0 + J'u + \frac{1}{2}J''u^2$ and $K(u) = K_0 + K'u + \frac{1}{2}K''u^2$. Here, the linear terms in u do not affect the phonon frequency. Therefore, we can expect the T dependence of ω_1 in the low-temperature regime to be

$$\omega_1^2 = \omega_A^2 + J''\sum_{i=1}^{N-1}\vec{M}_i \cdot \vec{M}_{i+1} - \frac{1}{2}K''\sum_{i=1}^{N}(\vec{M}_i \cdot \hat{z})^2. \tag{8}$$

In order to catch the main physics, we only consider a simple case [44], where $|\vec{M}_i(T)| = M(T)$, and M_i is parallel or antiparallel with the out-of-plane $\hat{z}$ direction (easy axis). Then, Eq. (8) can be rewritten as

$$\omega_1^2 = \omega_A^2 + \alpha M^2(T), \tag{9}$$

where α is given by $\alpha = (N-1)J'' - \frac{1}{2}NK''$. If $M(T)$ takes the form $M(T) = M_s(1 - T/T_N)^\beta$ [43], we can easily fit $f_1(T)$ using Eq. (9). As seen from Fig. 4(d), an excellent fit can be obtained with $\beta = 0.53 \pm 0.08$. Such β value is very consistent with the results measured by the reflectance magnetic circular dichroism [43]. Clearly, Eq. (9) indicates that the competition between J'' and K'' terms can lead to either $\alpha > 0$ or $\alpha < 0$. Due to J and K having thickness dependence, we can understand the contradicting softening and hardening effect observed in the few-layer and bulk samples [16,17], respectively. The spin-lattice coupling dominating the phonon renormalization may also inhibit the anharmonic effect, as manifested by the decay of coherent A_{1g}^1 mode (see Appendix C).

We note that the anomalous T-dependent f_1 below T_N could also be deduced by the phonon-assisted recombination characterized by τ_2, where the A_{1g}^1 phonon mode participates as the indirect scattering media and τ_2 shows anomaly near T_N. Unfortunately, due to the low signal-to-noise ratio, it is hard to discern if there is any anomaly appearing near T_N in the T-dependent phonon modes f_2 and f_3, as seen in Figs. 4(d) and 4(e).

IV. CONCLUSION

In conclusion, we performed ultrafast transient reflectivity measurements on $MnBi_2Te_4$. The experimental results show that the ultrafast nonequilibrium carrier and phonon dynamics can be strongly coupled to the long-range AFM order via the electron-magnon, electron-phonon, and spin-lattice interactions. In specific, the AFM transition at T_N in $MnBi_2Te_4$ creates an anomaly in the carrier and coherent phonon relaxation processes. It also causes an unusual phonon hardening of the f_1 mode relative to the values expected by the anharmonic phonon effect below T_N, and demonstrates the strong coupling between the AFM order and phonon.

ACKNOWLEDGMENTS

This work was supported by the National Key R&D Program of China (Grant No. 2022YFA1403002), the National Natural Science Foundation of China (Grants No. 92365102 and No. 62027807), and the Guangdong Basic and Applied Basic Research Foundation (Grant No. 2024A1515011600).

APPENDIX A: SAMPLE GROWTH AND CHARACTERIZATION

The sample was synthesized by the flux method. In the growth process, mixtures of Mn, Bi pieces, and Te shot in a molar ratio of 1:10:16 ($MnTe:Bi_2Te_3$ = 1:5) were placed in a 2-mL alumina growth crucible of a Canfield crucible set, and then sealed in a silica ampoule under approximately 1/3 atmosphere of argon gas. The sealed ampoule was heated to 900°C and held for 12 h. After slowly cooling across an ~ -10°C window below 600°C over 2 weeks, the excess flux was removed by centrifugation above the melting temperature of Bi_2Te_3 (585°C).

The sample was characterized by x-ray diffraction (XRD) and Raman spectroscopy, whose results are shown in Figs. 5 and 6. The XRD result shows the single-crystal diffraction pattern without impurity peaks, indicating the high quality of the crystals. Moreover, the Raman modes detected are consistent with the values reported in Ref. [16].

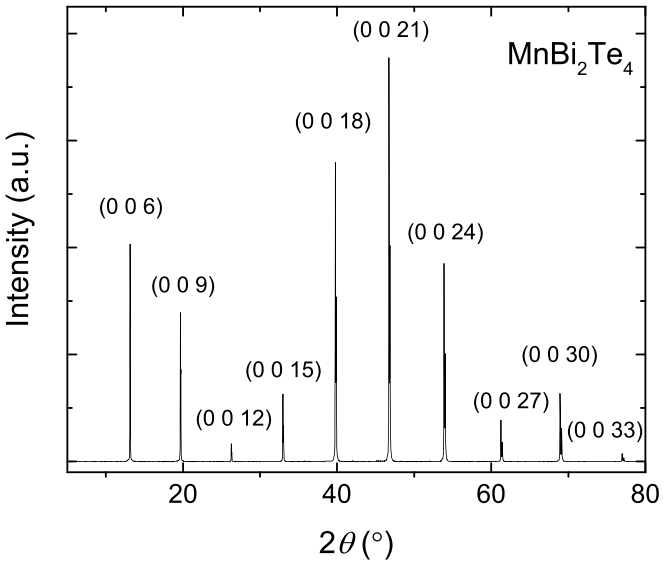

FIG. 5. X-ray diffraction data of the single-crystal $MnBi_2Te_4$ sample.

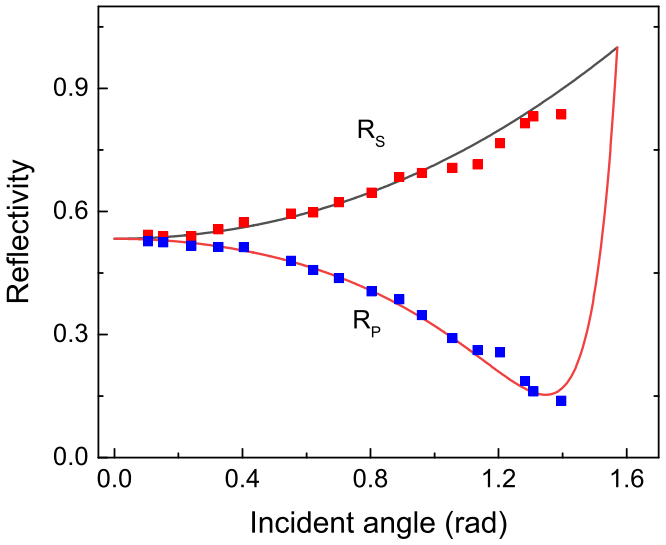

FIG. 7. Experimental reflectivities (800 nm) for *p*- and *s*-polarization as a function of the incident angle. The solid curves are the fitted values.

APPENDIX B: FITTING PROCEDURES VIA THE TWO-TEMPERATURE MODEL

In the two-temperature model [21,31], the e-ph relaxation time (τ_{e-ph}) is given by

$$\tau_{e-ph} = \frac{\gamma\left(T_e^2 - T_l^2\right)}{2H(T_e, T_l)}. \tag{B1}$$

Here, γ is the electron specific heat coefficient; T_e corresponds to the electron temperature after electron-electron (e-e) thermalization, which is initially higher than the lattice temperature T_l; and $H(T_e, T_l)$ is the energy transfer function, which takes the form

$$H(T_e, T_l) = f(T_e) - f(T_l), \tag{B2}$$

where

$$f(T) = 4g_\infty \frac{T^5}{\theta_D^4} \int_0^{\theta_D/T} \frac{x^4}{e^x - 1} dx, \tag{B3}$$

with θ_D and g∞ denoting the Debye temperature and the e-ph coupling constant, respectively. T_e can be calculated using

$$T_e = \left(T_l^2 + \frac{2U_l}{\gamma}\right)^{1/2}, \tag{B4}$$

where U_l is the deposited laser energy density. In the fitting process, γ, g_∞, and θ_D are determined as fitting parameters. Our fitted results, with $\theta_D \approx 340$ K, agree well with the experimental data above ~80 K, and hence strongly support our initial assignment of τ_1 to the relaxation based on e-ph interaction. The electron temperature T_e obtained here is also used for fitting τ_1 via Eq. (2) in the main text.

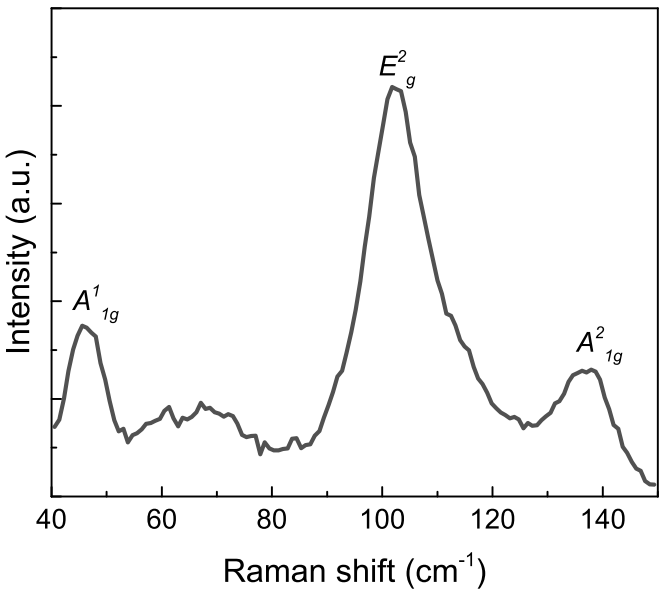

FIG. 6. Raman spectroscopy of the $MnBi_2Te_4$ sample measured at room temperature.

APPENDIX C: EXTRA EXPERIMENTAL DATA

To determine the pump light (800-nm) penetration depth, We performed a static reflectivity measurement. The reflectivities for *p*- and *s*-polarized light (R_P, R_S) were measured as functions of the incident angle. The experimental data and the fitting results using the complex Fresnel equations for lossy materials are shown in Fig. 7(a). According to the fitting results, we extracted the real and imaginary parts of the refractive index ($\tilde{N} = n + ik$), which are $n \simeq 3.23$ and $k \simeq 3.13$, respectively. The latter gives a penetration depth of ~20.3 nm, which is consistent with other topological materials [22,45]. If we consider the thickness of ~1.4 nm for one layer, the depth of our pump and probe region can be calculated as ~14.5 layers.

The phonon decay rate of the A_{1g}^1 mode extracted from the damped harmonic oscillators is shown in Fig. 8, and the abrupt change at T_N reflects the influence of magnetic phase transition on the spin-lattice interaction.

APPENDIX D: ADDITIONAL DISCUSSIONS OF τ_{long}

We assign the τ_{long} process to the spin-lattice coupling because (1) such process disappears at $T > T_N$, which reflects its long-range magnetic order origin; (2) because its timescale is about 1 ns, the related energy scale of corresponding collective modes should be quite small, i.e., acoustic phonons and magnons. Since the acoustic phonon exists at all temperatures, it solely cannot explain the emergence of this long-rise component below T_N.

We note that applying a strong magnetic field with several tesla might be able to alter the long-range magnetic order, and possibly can further change the long-rise component (or the pump-probe signal), which needs more exploration in the future.

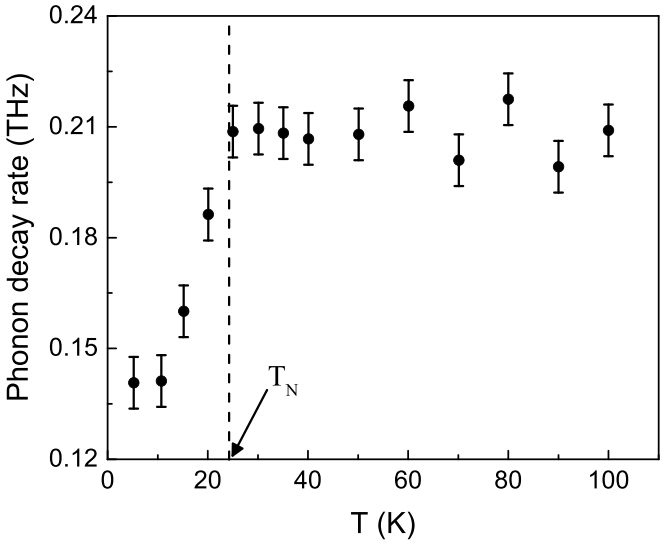

FIG. 8. Phonon decay rate of A_{1g}^1 mode as a function of temperature.

[1] B. A. Bernevig, C. Felser, and H. Beidenkopf, Progress and prospects in magnetic topological materials, Nature (London) **603**, 41 (2022).

[2] M. Gibertini, M. Koperski, A. F. Morpurgo, and K. S. Novoselov, Magnetic 2D materials and heterostructures, Nat. Nanotechnol. **14**, 408 (2019).

[3] A. Kirilyuk, A. V. Kimel, and T. Rasing, Ultrafast optical manipulation of magnetic order, Rev. Mod. Phys. **82**, 2731 (2010).

[4] L. Šmejkal, Y. Mokrousov, B. Yan, and A. H. MacDonald, Topological antiferromagnetic spintronics, Nat. Phys. **14**, 242 (2018).

[5] M. M. Otrokov *et al.*, Prediction and observation of an antiferromagnetic topological insulator, Nature (London) **576**, 416 (2019).

[6] D. S. Lee, T. H. Kim, C. H. Park, C. Y. Chung, Y. S. Lim, W. S. Seo, and H. H. Park, Crystal structure, properties and nanostructuring of a new layered chalcogenide semiconductor, Bi_2MnTe_4, CrystEngComm **15**, 5532 (2013).

[7] C. Liu, Y. Wang, H. Li, Y. Wu, Y. Li, J. Li, K. He, Y. Xu, J. Zhang, and Y. Wang, Robust axion insulator and Chern insulator phases in a two-dimensional antiferromagnetic topological insulator, Nat. Mater. **19**, 522 (2020).

[8] A. Zeugner *et al.*, Chemical aspects of the candidate antiferromagnetic topological insulator $MnBi_2Te_4$, Chem. Mater. **31**, 2795 (2019).

[9] Y. Gong *et al.*, Experimental realization of an intrinsic magnetic topological insulator, Chin. Phys. Lett. **36**, 076801 (2019).

[10] M. Z. Hasan and C. L. Kane, *Colloquium*: Topological insulators, Rev. Mod. Phys. **82**, 3045 (2010).

[11] J. Li, Y. Li, S. Du, Z. Wang, B.-L. Gu, S.-C. Zhang, K. He, W. Duan, and Y. Xu, Intrinsic magnetic topological insulators in van der Waals layered $MnBi_2Te_4$-family materials, Sci. Adv. **5**, eaaw5685 (2019).

[12] D. Zhang, M. Shi, T. Zhu, D. Xing, H. Zhang, and J. Wang, Topological axion states in the magnetic insulator $MnBi_2Te_4$ with the quantized magnetoelectric effect, Phys. Rev. Lett. **122**, 206401 (2019).

[13] M. M. Otrokov, I. P. Rusinov, M. Blanco-Rey, M. Hoffmann, A. Y. Vyazovskaya, S. V. Eremeev, A. Ernst, P. M. Echenique, A. Arnau, and E. V. Chulkov, Unique thickness-dependent properties of the van der Waals interlayer antiferromagnet $MnBi_2Te_4$ films, Phys. Rev. Lett. **122**, 107202 (2019).

[14] J.-Q. Yan, Q. Zhang, T. Heitmann, Z. Huang, K. Y. Chen, J.-G. Cheng, W. Wu, D. Vaknin, B. C. Sales, and R. J. McQueeney, Crystal growth and magnetic structure of $MnBi_2Te_4$, Phys. Rev. Mater. **3**, 064202 (2019).

[15] M. Mogi, M. Kawamura, R. Yoshimi, A. Tsukazaki, Y. Kozuka, N. Shirakawa, K. S. Takahashi, M. Kawasaki, and Y. Tokura, A magnetic heterostructure of topological insulators as a candidate for an axion insulator, Nat. Mater. **16**, 516 (2017).

[16] H. Padmanabhan, M. Poore, P. K. Kim, N. Z. Koocher, V. A. Stoica, D. Puggioni, H. Wang, X. Shen, A. H. Reid, M. Gu, M. Wetherington, S. H. Lee, R. D. Schaller, Z. Mao, A. M. Lindenberg, X. Wang, J. M. Rondinelli, R. D. Averitt, and V. Gopalan, Interlayer magnetophononic coupling in $MnBi_2Te_4$, Nat. Commun. **13**, 1929 (2022).

[17] J. Choe, D. Lujan, M. Rodriguez-Vega, Z. Ye, A. Leonardo, J. Quan, T. N. Nunley, L.-J. Chang, S.-F. Lee, J. Yan, G. A. Fiete, R. He, and X. Li, Electron–phonon and spin–lattice coupling in atomically thin layers of $MnBi_2Te_4$, Nano Lett. **21**, 6139 (2021).

[18] F. M. Bartram, Y.-C. Leng, Y. Wang, L. Liu, X. Chen, H. Peng, H. Li, P. Yu, Y. Wu, M.-L. Lin, J. Zhang, P.-H. Tan, and L. Yang, Ultrafast coherent interlayer phonon dynamics in atomically thin layers of $MnBi_2Te_4$, npj Quantum Mater. **7**, 84 (2022).

[19] J. Qi, X. Chen, W. Yu, P. Cadden-Zimansky, D. Smirnov, N. H. Tolk, I. Miotkowski, H. Cao, Y. P. Chen, Y. Wu, S. Qiao, and Z.

Jiang, Ultrafast carrier and phonon dynamics in Bi_2Se_3 crystals, Appl. Phys. Lett. **97**, 182102 (2010).

[20] Y.-P. Lai, H.-J. Chen, K.-H. Wu, and J.-M. Liu, Temperature-dependent carrier–phonon coupling in topological insulator Bi_2Se_3, Appl. Phys. Lett. **105**, 232110 (2014).

[21] L. Cheng, C. La-o-vorakiat, C. S. Tang, S. K. Nair, B. Xia, L. Wang, J.-X. Zhu, and E. E. M. Chia, Temperature-dependent ultrafast carrier and phonon dynamics of topological insulator $Bi_{1.5}Sb_{0.5}Te_{1.8}Se_{1.2}$, Appl. Phys. Lett. **104**, 211906 (2014).

[22] M. C. Wang, S. Qiao, Z. Jiang, S. N. Luo, and J. Qi, Unraveling photoinduced spin dynamics in the topological insulator Bi_2Se_3, Phys. Rev. Lett. **116**, 036601 (2016).

[23] D. J. Hilton and C. L. Tang, Optical orientation and femtosecond relaxation of spin-polarized holes in GaAs, Phys. Rev. Lett. **89**, 146601 (2002).

[24] Y. M. Dai, J. Bowlan, H. Li, H. Miao, S. F. Wu, W. D. Kong, P. Richard, Y. G. Shi, S. A. Trugman, J.-X. Zhu, H. Ding, A. J. Taylor, D. A. Yarotski, and R. P. Prasankumar, Ultrafast carrier dynamics in the large-magnetoresistance material WTe_2, Phys. Rev. B **92**, 161104(R) (2015).

[25] L. Cheng, F. C. Fei, H. Hu, Y. M. Dai, F. Q. Song, and J. Qi, Ultrafast carrier and lattice dynamics in the Dirac semimetal $NiTe_2$, Phys. Rev. B **106**, 104308 (2022).

[26] N. Thielemann-Kühn, D. Schick, N. Pontius, C. Trabant, R. Mitzner, K. Holldack, H. Zabel, A. Föhlisch, and C. Schüßler-Langeheine, Ultrafast and energy-efficient quenching of spin order: Antiferromagnetism beats ferromagnetism, Phys. Rev. Lett. **119**, 197202 (2017).

[27] L. Rettig, R. Cortés, S. Thirupathaiah, P. Gegenwart, H. S. Jeevan, M. Wolf, J. Fink, and U. Bovensiepen, Ultrafast momentum-dependent response of electrons in antiferromagnetic $EuFe_2As_2$ driven by optical excitation, Phys. Rev. Lett. **108**, 097002 (2012).

[28] E. Carpene, E. Mancini, C. Dallera, M. Brenna, E. Puppin, and S. De Silvestri, Dynamics of electron-magnon interaction and ultrafast demagnetization in thin iron films, Phys. Rev. B **78**, 174422 (2008).

[29] J. Qi, L. Yan, H. D. Zhou, J.-X. Zhu, S. A. Trugman, A. J. Taylor, Q. X. Jia, and R. P. Prasankumar, Coexistence of coupled magnetic phases in epitaxial $TbMnO_3$ films revealed by ultrafast optical spectroscopy, Appl. Phys. Lett. **101**, 122904 (2012).

[30] J. Ning, Y. Zhu, J. Kidd, Y. Guan, Y. Wang, Z. Mao, and J. Sun, Subtle metastability of the layered magnetic topological insulator $MnBi_2Te_4$ from weak interactions, npj Comput. Mater. **6**, 157 (2020).

[31] R. H. M. Groeneveld, R. Sprik, and A. Lagendijk, Femtosecond spectroscopy of electron-electron and electron-phonon energy relaxation in Ag and Au, Phys. Rev. B **51**, 11433 (1995).

[32] D. K. Schroder, *Semiconductor Material and Device Characterization* (Wiley, New York, 2005).

[33] Y. M. Sheu, Y. J. Chien, C. Uher, S. Fahy, and D. A. Reis, Free-carrier relaxation and lattice heating in photoexcited bismuth, Phys. Rev. B **87**, 075429 (2013).

[34] P. Li, J. Yu, Y. Wang, and W. Luo, Electronic structure and topological phases of the magnetic layered materials $MnBi_2Te_4$, $MnBi_2Se_4$, and $MnSb_2Te_4$, Phys. Rev. B **103**, 155118 (2021).

[35] A. Vaterlaus, T. Beutler, and F. Meier, Spin-lattice relaxation time of ferromagnetic gadolinium determined with time-resolved spin-polarized photoemission, Phys. Rev. Lett. **67**, 3314 (1991).

[36] Y. Yuan, P. Kissin, D. Puggioni, K. Cremin, S. Lei, Y. Wang, Z. Mao, J. M. Rondinelli, R. D. Averitt, and V. Gopalan, Ultrafast quasiparticle dynamics in the correlated semimetal $Ca_3Ru_2O_7$, Phys. Rev. B **99**, 155111 (2019).

[37] E. E. M. Chia, J.-X. Zhu, D. Talbayev, R. D. Averitt, A. J. Taylor, K.-H. Oh, I.-S. Jo, and S.-I. Lee, Observation of competing order in a high-T_c superconductor using femtosecond optical pulses, Phys. Rev. Lett. **99**, 147008 (2007).

[38] E. Beaurepaire, J.-C. Merle, A. Daunois, and J.-Y. Bigot, Ultrafast spin dynamics in ferromagnetic nickel, Phys. Rev. Lett. **76**, 4250 (1996).

[39] Z. S. Aliev, I. R. Amiraslanov, D. I. Nasonova, A. V. Shevelkov, N. A. Abdullayev, Z. A. Jahangirli, E. N. Orujlu, M. M. Otrokov N. T. Mamedov, M. B. Babanly, and E. V. Chulkov, Novel ternary layered manganese bismuth tellurides of the $MnTe$-Bi_2Te_3 system: Synthesis and crystal structure, J. Alloys Compd. **789**, 443 (2019).

[40] Y. P. Liu, Y. J. Zhang, J. J. Dong, H. Lee, Z. X. Wei, W. L. Zhang, C. Y. Chen, H. Q. Yuan, Y. F. Yang, and J. Qi, Hybridization dynamics in $CeCoIn_5$ revealed by ultrafast optical spectroscopy, Phys. Rev. Lett. **124**, 057404 (2020).

[41] M. Balkanski, R. F. Wallis, and E. Haro, Anharmonic effects in light scattering due to optical phonons in silicon, Phys. Rev. B **28**, 1928 (1983).

[42] J. Menéndez and M. Cardona, Temperature dependence of the first-order Raman scattering by phonons in Si, Ge, and α-Sn: Anharmonic effects, Phys. Rev. B **29**, 2051 (1984).

[43] S. Yang, X. Xu, Y. Zhu, R. Niu, C. Xu, Y. Peng, X. Cheng, X. Jia, Y. Huang, X. Xu, J. Lu, and Y. Ye, Odd-even layer-number effect and layer-dependent magnetic phase diagrams in $MnBi_2Te_4$, Phys. Rev. X **11**, 011003 (2021).

[44] K. He, $MnBi_2Te_4$-family intrinsic magnetic topological materials, npj Quantum Mater. **5**, 90 (2020).

[45] Y. Gao, S. Kaushik, E. J. Philip, Z. Li, Y. Qin, Y. P. Liu, W. L. Zhang, Y. L. Su, X. Chen, H. Weng, D. E. Kharzeev, M. K. Liu, and J. Qi, Chiral terahertz wave emission from the Weyl semimetal TaAs, Nat. Commun. **11**, 720 (2020).